Editors' Suggestion

Electrical control of the *g* tensor of the first hole in a silicon MOS quantum dot

S. D. Liles [1,*] F. Martins [1,2] D. S. Miserev,[1,3] A. A. Kiselev,[4] I. D. Thorvaldson,[1] M. J. Rendell,[1] I. K. Jin,[1]
F. E. Hudson [5] M. Veldhorst,[5,6] K. M. Itoh,[7] O. P. Sushkov [1] T. D. Ladd [1,4] A. S. Dzurak [5] and A. R. Hamilton [1]

[1]*School of Physics, University of New South Wales, Sydney, New South Wales 2052, Australia*
[2]*Hitachi Cambridge Laboratory, J. J. Thomson Avenue, Cambridge CB3 0HE, United Kingdom*
[3]*Department of Physics, University of Basel, Klingelbergstrasse 82, CH-4056 Basel, Switzerland*
[4]*HRL Laboratories, LLC, 3011 Malibu Canyon Road, Malibu, California 90265, USA*
[5]*School of Electrical Engineering and Telecommunications, University of New South Wales, Sydney, New South Wales 2052, Australia*
[6]*QuTech and Kavli Institute of Nanoscience, TU Delft, 2600 GA Delft, The Netherlands*
[7]*School of Fundamental Science and Technology, Keio University, Yokohama 223-8522, Japan*

Single holes confined in semiconductor quantum dots are a promising platform for spin-qubit technology, due to the electrical tunability of the *g* factor of holes. However, the underlying mechanisms that enable electric spin control remain unclear due to the complexity of hole-spin states. Here, we study the underlying hole-spin physics of the first hole in a silicon planar metal-oxide-semiconductor (MOS) quantum dot. We show that nonuniform electrode-induced strain produces nanometer-scale variations in the heavy-hole–light-hole (HH-LH) splitting. Importantly, we find that this nonuniform strain causes the HH-LH splitting to vary by up to 50% across the active region of the quantum dot. We show that local electric fields can be used to displace the hole relative to the nonuniform strain profile, allowing a mechanism for electric modulation of the hole *g* tensor. Using this mechanism, we demonstrate tuning of the hole *g* factor by up to 500%. In addition, we observe a potential sweet spot where $dg_{(1\bar{1}0)}/dV = 0$, offering a configuration to suppress spin decoherence caused by electrical noise. These results open a path towards a technology involving engineering of nonuniform strains to optimize spin-based devices.

DOI: 10.1103/PhysRevB.104.235303

I. INTRODUCTION

Single-hole spins confined in group IV quantum dots provide a promising path towards scalable quantum computing [1–4]. These devices can leverage well-established industrial platforms [5,6], while also enabling rapid all-electric spin control [7–10]. Recent demonstrations have included single-qubit gate operations of holes in silicon devices [10] and up to four-qubit gate operations of holes in Ge devices [11–15].

When developing spin-qubit technology, a fundamental question arises: What defines the coupling of a single isolated spin to the external magnetic field? While this has been well studied for electrons [2,16], the complexity of hole-spin states makes this a nontrivial question [17–22]. Holes occupy the valence band, which originates from $l = 1$ atomic *p* orbitals, with an effective spin of $S = \frac{3}{2}$ and a strong intrinsic spin-orbit coupling. For qubit devices, the combination of spin-orbit coupling and quantum confinement strongly modifies the hole-spin properties, which become sensitive to the size and shape of the quantum dot [23,24]. In addition, the degree of mixing between the heavy hole (HH, $m_j = \pm 3/2$) and light hole (LH, $m_j = \pm 1/2$) subbands leads to a mixed spin character. This causes holes' spins to be very sensitive to effects

that alter the HH-LH splitting, such as crystal anisotropies, strain, and the confinement profile [21,25,26].

The *g* tensor is the key parameter for studying the coupling of a spin-orbit state to a magnetic field [26–33]. However, most studies of the *g* tensor of hole quantum dots have been performed using devices that confine an unknown number of holes [34–41]. This has hindered the ability to understand hole-spin-qubit devices, since the number of holes is a primary factor influencing the orbital physics of the quantum dot [42]. It is imperative to know the quantum dot orbital wave-function shape in order to make any quantitative comparison between experiments and theory, or to compare between different device designs or material systems.

Here, we study the spin properties of the first hole confined in a planar silicon metal-oxide-semiconductor (MOS) quantum dot [43–46]. By operating the device in the single-charge ($N = 1$) regime, we characterize the *g* tensor in a known charge state with a well-defined quantum dot orbital index. This allows direct comparisons between experimental results and theoretical modeling, while the simple planar geometry allows the contributions of competing effects such as orbital alignment and nonuniform electrode-induced strain to be separated [47,48].

Our results show that electrode-induced strain is key in mediating electric *g*-factor control in these hole MOS quantum dots. The effect of nonuniform electrode-induced strain on the hole *g* tensor is considered here for hole-spin qubits. Therefore
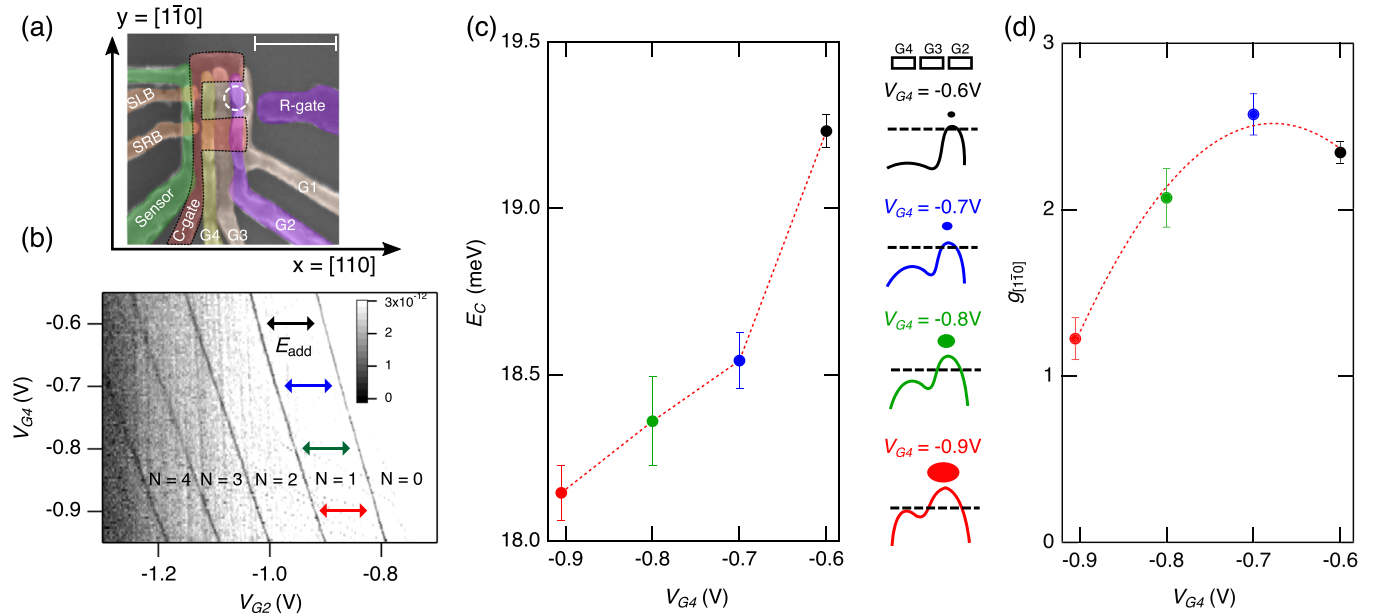
FIG. 1. A single hole in a silicon quantum dot. (a) False-color SEM image of a device gate stack. A single quantum dot is formed in the region indicated by the white dashed circle by using gate G2 as the quantum dot plunger gate, while gates G1 and G3 and the C gate provide the electrostatic confinement. SLB and SRB are the left and right sensor barrier gates, respectively. The in-plane crystal orientations are indicated, where the sample x axis is the crystal axis [110] and the sample y axis is the crystal axis [1$\bar{1}$0]. The out-of-plane direction is the sample z axis, corresponding to crystal axis [001]. The horizontal white scale bar is 250 nm. (b) Charge stability diagram showing operation down to the last hole, where the grayscale is dI_{sens}/dV_{G2}. A series of charge transitions can be observed as negative spikes in dI_{sens}/dV_{G2}. (c) The charging energy E_C measured at the V_{G4} indicated by the colored horizontal arrows in (b). Schematics on the right indicate a line cut of the electrostatic potential energy along the sample x axis. A hole quantum dot is formed at the potential maxima. The black horizontal dashed line indicates the Fermi energy, and the ellipse above each schematic represents the single-hole probability density, which is displaced and elongated as V_{G4} finely tunes the local electrostatic environment. (d) The measured effective g factor for a magnetic field applied along the sample y axis [1$\bar{1}$0]. The dashed red line is a guide to the eye.

these results open a platform for hole-spin-qubit technology where the hole-spin qubits can be electrically manipulated by displacing the wave function relative to precisely engineered electrode-induced strain gradients.

II. RESULTS

A. Isolating a single hole

The device studied in this paper was fabricated on an isotopically enriched ^{28}Si substrate with a high-quality 5.9-nm SiO$_2$ gate oxide. The device consists of a planar multilayer aluminum gate stack [43,49]. Figure 1(a) shows a scanning electron microscopy (SEM) image of the device layout. This layout allows the formation of a stable single-hole quantum dot in the region indicated by the white circle [46]. The top gate of the adjacent charge sensor is indicated in green in Fig. 1(a). By independently monitoring the current through the charge sensor (I_{sens}), we can unambiguously identify the absolute number of holes occupying the quantum dot. Further details are provided in Appendix A.

Figure 1(b) presents the charge stability diagram of the device, which was obtained by monitoring the transconductance (dI_{sens}/dV_{G2}) of the charge sensor. The stability diagram shows a series of charge transitions, consistent with a single quantum dot formed under G2, with the number of holes indicated as N. Beyond the region labeled $N = 0$, no further

charge transitions were observed, confirming that the device was operating down to the last hole.

Figure 1(c) shows the Coulomb charging energy for the $N = 1$ to $N = 2$ transition, measured at different values of V_{G4} (see Appendix B for full details). For a fixed number of holes, the Coulomb charging energy E_C is inversely proportional to the size of the quantum dot confinement [42]. In Fig. 1(c), E_C increases as V_{G4} is made more positive, consistent with the quantum dot becoming smaller. Therefore, in the region between the first and second Coulomb peaks [indicated by the colored arrows in Fig. 1(b)], it is possible to confine a single hole and use V_{G4} to finely tune the spatial extent of the hole wave function.

The remainder of this paper focuses on the g factor of the first ($N = 1$) hole confined in this planar quantum dot. The hole occupies the lowest-energy orbital state, avoiding complications from higher quantum dot orbitals.

B. Electrical modulation of the $N = 1$ hole g factor

We examined the g factor of the first hole as the shape of the wave function was systematically varied using the bias of a nearby electrode (G4). The effective hole g factor was extracted from the linear increase in the $N = 1$ addition energy with magnetic field B (see Sec. S5 of the Supplemental Material [50]). The in-plane magnetic field was aligned with the sample y axis (crystal axis [1$\bar{1}$0]). Figure 1(d) presents the

single-hole effective g factor ($g_{1\bar{1}0}$) for different electrostatic confinement profiles. The magnitude of $g_{1\bar{1}0}$ can be tuned between 1.2 ± 0.1 and 2.6 ± 0.1 with only a small change in V_{G4}. From the maximum slope of Fig. 1(d) we obtain the maximum electric control over the g factor as $dg/dV_{G4} = 8.1 \pm 0.2$ V^{-1} (for this specific in-plane magnetic field orientation). The observed dg/dV_G for holes is six orders of magnitude larger than dg/dV_G for electrons in identical silicon MOS devices [33] and is comparable to dg/dV_G observed for holes in other group IV quantum dots [34,51]. Based on the maximum dg/dV_{G4} we estimate a minimum Rabi frequency of 40 MHz [34,36,52] (see Appendix D); however, a full characterization of the Rabi frequency requires a more detailed study [34].

A key result of Fig. 1(d) is the observation of a potential "sweet spot" around $V_{G4} = -0.7$ V, where $dg_y/dV_{G4} = 0$ (identification of a "global sweet spot" would require characterization of dg/dV over the full gate parameter space). Sweet spots where $d\overleftrightarrow{g}/dV_G = 0$ V^{-1} are important for qubits since the coupling between the spin and electric fluctuations in the voltage source (V_G) are suppressed. Minimizing the effects of charge noise is critical for hole-spin qubits since the coherence time T_2^* of hole spins in group IV quantum dots is primarily limited by electrical noise [14,53]. Furthermore, recent theoretical work shows that it is possible to engineer sweet spots where the dominant charge dephasing mechanism is suppressed while still allowing high-speed electrical qubit control [54–56].

C. Characterizing the *g* tensor

In hole systems, the coupling to a magnetic field is influenced by many factors, such as the three-dimensional (3D) wave-function shape, the local strain, and the crystal anisotropy [23,24]. Fully defining the magnetic response to a magnetic field ($\vec{B}$) requires a 3×3 g tensor with six free parameters. The g tensor is defined as

$$\overleftrightarrow{g} = R(\vartheta_0, \phi_0, \theta_0) \begin{pmatrix} g_1 & 0 & 0 \\ 0 & g_2 & 0 \\ 0 & 0 & g_3 \end{pmatrix} R^{-1}(\vartheta_0, \phi_0, \theta_0), \quad (1)$$

where the angles ϑ_0, ϕ_0, and θ_0 define the orientation of the principal magnetic axes with respect to the sample (x, y, z) axes and g_1, g_2, and g_3 define the principal g factors. The R matrix represents the effect of three consecutive rotations around the sample axes (as described in Appendix B).

Experimental characterization of the g tensor requires measurements of the g factor for a range of magnetic field orientations in all three dimensions. In this paper, the g tensor of the $N = 1$ hole was characterized experimentally using a vector magnet. The magnetic field was fixed at $|\vec{B}| = 1$ T, and a 2π rotation in increments of $\pi/24$ around the sample x, y, and z axes was performed. At each magnetic field orientation we extracted the g factor from the linear change of the $N = 1$ addition energy. The measurement was repeated for two different confinement profiles, which were controlled by setting $V_{G4} = -0.9$ V [Fig. 2(a-i)] or $V_{G4} = -0.7$ V [Fig. 2(b-i)]. The solid lines in Figs. 2(a-i) and 2(b-i) show the best fit of the full data set (all 144 points) to Eq. (1). The best-fit parameters for both confinement profiles are presented in Table I.
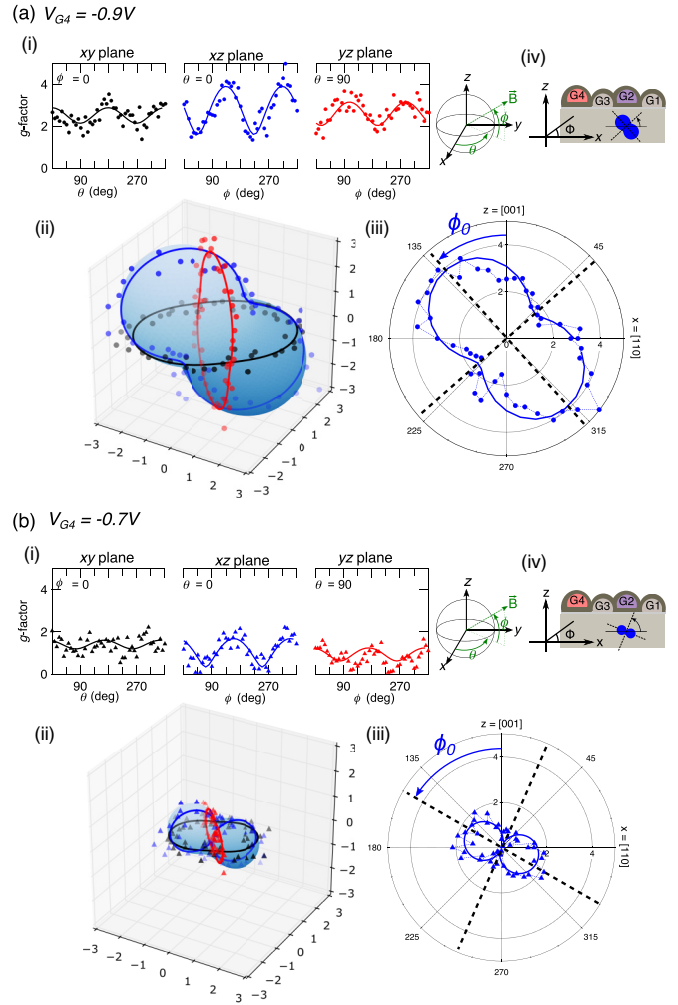

FIG. 2. Electrical control of the g-tensor orientation. Measurements of the hole g tensor for (a) $V_{G4} = -0.9$ V and (b) $V_{G4} = -0.7$ V. (i) The measured effective g factor for magnetic field rotations around the sample z (black), y (blue), and x (red) axes. Solid lines are a best fit of all data to Eq. (1). Typical uncertainty in the g factor is 0.4; see Sec. S5.2 of the Supplemental Material [50]. Angles θ and φ define the orientation of the magnetic field $\vec{B}$ as indicated on the adjacent sphere. (ii) The shaded blue surface is the 3D g-tensor surface defined by the appropriate parameters in Table I. For reference the experimental data (circles or triangles) and best fit (solid lines) from (i) are included. (iii) Reproduction of the g-factor measurements for the y-axis rotation (blue) ($\theta = 0$) as a polar plot. The radial axis is $|g|$, while the angle corresponds to φ. The axes of symmetry of the g tensor in the xz plane are indicated by the dashed black lines. The magnitude of the tilting into the x plane is indicated by the blue arrow, where the tilt in the xz plane corresponds to ϕ_0 of Eq. (1). (iv) The sample schematic with the xz g-tensor surface, highlighting the tilted g-tensor orientation with respect to the Si/SiO$_2$ interface. Circles (triangles) are used for raw data in (a) [in (b)].

Figures 2(a-ii) and 2(b-ii) present a 3D visualization of the best-fit g tensor.

For the case of $V_{G4} = -0.9$ V, the largest principal g factor (g_3) is 3.9 ± 0.1, and the smallest principal g factor (g_1) is 1.4 ± 0.2. The orientation of the g tensor is distinctly tilted with respect to the sample axes [Fig. 2(a-ii)], such that the

TABLE I. Principal g factors for a single hole in a silicon quantum dot, measured at two different confinement (V_{G4}) potentials. The values are extracted by fitting the respective data set in Fig. 2 to Eq. (1). See Appendix E for the fitting procedure.

Parameter	$V_{G4} = -0.9$ V	$V_{G4} = -0.7$ V
g_1	1.4 ± 0.2	0.3 ± 0.2
g_2	2.3 ± 0.1	1.0 ± 0.1
g_3	3.9 ± 0.1	1.7 ± 0.1
ϑ_0	$19° \pm 7°$	$10° \pm 9°$
ϕ_0	$42° \pm 2°$	$70° \pm 3°$
θ_0	$9° \pm 3°$	$-20° \pm 6°$

principal magnetic axes are not aligned with any lithographic or crystallographic axes of the sample. To demonstrate this tilted orientation, Fig. 2(a-iii) shows the measured g factor around the sample y axis on polar axes. In particular, we note that the g tensor is tilted by $\phi_0 = 42° \pm 2°$ in the xz plane. Figure 2(a-iv) shows a schematic of the g-tensor surface in the xz plane of the sample, highlighting that the largest g factor occurs when the magnetic field is tilted by $42°$ away from the Si/SiO$_2$ interface. The observation that the principal axes of the g tensor are not fixed by any sample axes is the key result of the g-tensor characterization in Fig. 2(a).

We next investigate whether the orientation of the g-tensor principal axes can be electrically tuned. The hole wavefunction shape was changed by varying V_{G4} from -0.9 to -0.7 V, while at the same time making V_{G2} more negative. The net effect is to strengthen the electrostatic confinement along the sample x direction. For the case of $V_{G4} = -0.7$ V, the maximum principal g factor (g_3) is 1.7 ± 0.1, while the minimum principal g factor (g_1) is 0.3 ± 0.2. By comparing the 3D g-tensor surfaces in Figs. 2(a-ii) and 2(b-ii) it is clear that both the size and orientation of the g tensor are sensitive to V_{G4}. To demonstrate the observed change in g-tensor orientation, Fig. 2(b-iii) reproduces the g factor around the y axis. For $V_{G4} = -0.7$ V we highlight that the tilting into the sample xz plane is now $\phi_0 = 70° \pm 3°$, compared with $\phi_0 = 42° \pm 2°$ for $V_{G4} = -0.9$ V. The observation that the orientation of the principal axes is strongly affected by the gate bias, even for a single hole, is the key result of the g-tensor data set presented in Fig. 2(b).

D. Numerical simulations of the single-hole g tensor

To explore the physical origins of the g-tensor magnitude and orientation, we perform detailed three-dimensional modeling of the device, including (i) the real lithographic gate stack determined from design and device microscopy, (ii) strain buildup accompanying cooldown to cryogenic temperatures, (iii) self-consistent electrostatics with holes accumulating at the Si/SiO$_2$ interface at experimentally applied gate biases, and (iv) quantum mechanics of the Si complex valence band (parametrized via the 6×6 Luttinger-Kohn Hamiltonian with Bir-Pikus coupling to the lattice strain).

In systems with strong spin-orbit coupling, the confinement and spin properties are inextricably linked. Therefore we begin the modeling of the hole g tensor by first investigating the hole confinement profile. Figure 3(a) shows the calculated
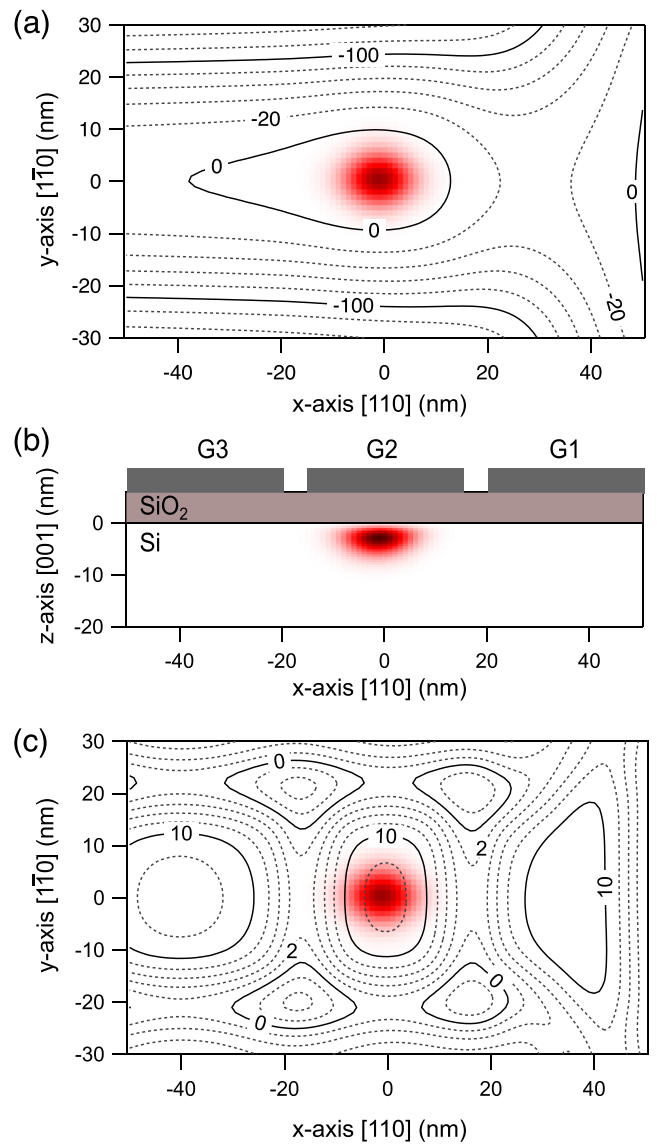
FIG. 3. Numerical simulations of the electrostatic confinement, strain, and single-hole eigenstates. (a) Electrostatic confinement profile (contour lines) and hole ground-state probability density (color map) in the xy plane. The contours are spaced by 20 meV. The in-plane confinement is strongest along the sample y axis [1$\bar{1}$0], consistent with the strong influence of the large C gate. Confinement along the sample x axis (crystal [110] axis) is weaker and is provided by gates G1 and G3. This simulation is for the experimentally applied voltages, as described in Appendix C. (b) Hole probability density in the sample xz plane. The footprint of each gate is shown (the vertical height of the Al gates is 30+ nm). (c) Spatial profile of the strain-induced HH-LH splitting in energy, with the hole probability density overlaid as a red color map and HH-LH splitting shown as contours spaced by 2 meV.

electrostatic confinement potential in the xy plane. The hole ground-state probability density projected to the same plane is overlaid as a color map in Fig. 3(a). Similarly, Fig. 3(b) shows the hole probability density projected to the sample xz plane. The hole ground state is mostly heavy hole (HH) in character. The vertical extent of the wave function is ~ 7 nm, and the diameter is ~ 30 nm, consistent with the diameter estimated
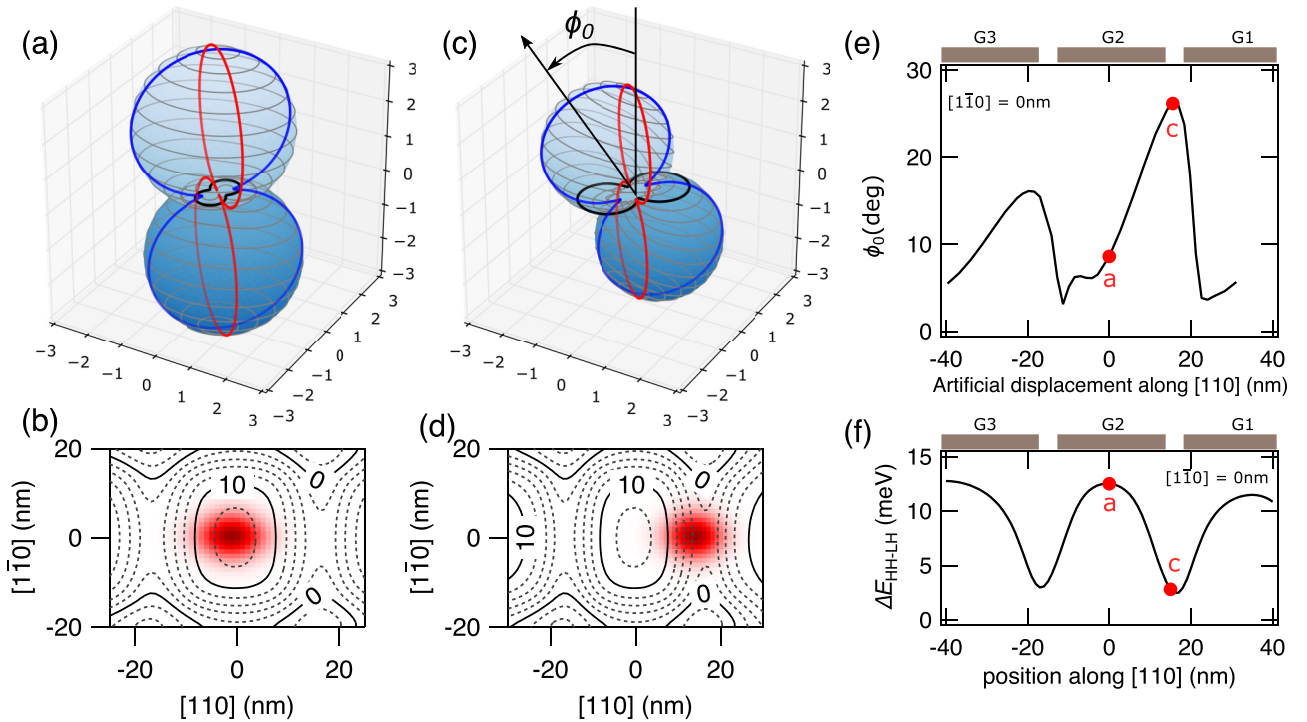
FIG. 4. Tilted *g* tensor and electrode-induced strain. (a) Simulated *g*-tensor surface for the wave-function position and strain profile indicated in (b). The hole is localized directly below the G2 gate, where the local strain gradients are low and shear strains are minimal. The orientation of the *g* tensor is primarily defined by the orientation of the confinement, with the largest *g* factor occurring for approximately out-of-plane magnetic field; more details are given in (e). The intersection of the *g*-tensor surface with the sample *xy* (black), *xz* (blue), and *yz* (red) planes is indicated by the respective solid lines. (c) Same as (a), except forcing the hole to the position indicated in (d). The contour lines in (b) and (d) are spaced by 2 meV. (e) The *g*-tensor tilting ϕ_0 as a function of the artificial shift of the electrostatic confinement along the sample *x* axis. Red circles indicate the *x*-axis position and ϕ_0 value for the cases in (a) and (c). Above (e) we schematically indicate the location of gates G1, G2, and G3. We find that the regions near gate edges correspond to the regions of largest tilting ϕ_0. (f) The simulated strain-induced $\Delta_{\text{HH-LH}}$ for a line cut along the *x* axis. The $\Delta_{\text{HH-LH}}$ is not symmetric along the sample *x* axis, since the lithography and confinement potential are not symmetric along the sample *x* axis (see Fig. 3).

from the measured charging energy in Fig. 1(d) (see Sec. S6 of the Supplemental Material [50]). Therefore the holes are confined in a thin disklike wave function, which is pulled tightly against the Si/SiO$_2$ interface. The axis of strongest orbital confinement is out of plane with respect to the Si/SiO$_2$ interface.

Holes confined to a simple 2D-like geometry will have the primary magnetic axis aligned with the axis of strongest confinement [17,20,31]. One might therefore expect our disklike hole wave function to have the largest *g* factor for an out-of-plane magnetic field, corresponding to $\phi_0 \approx 0$. However, the experimental results in Fig. 2 show that the largest *g* factor is strongly tilted away from the axis of strongest confinement, with $\phi_0 > 40°$.

A nonzero ϕ_0 could, in principle, be caused by a drastic rotation of the axis of strongest confinement, due to a complete change in the electrostatic confinement potential (see Sec. S3 of the Supplemental Material [50]). However, detailed numeric simulations show that no reasonable range of gate voltages, interface steps, or surfaces charges can produce a substantial tilting of the out-of-plane confinement orientation. For all reasonable configurations, the single-hole confinement in this MOS device is most strongly defined by the vertical hard wall potential of the Si/SiO$_2$ interface. Something other than electrostatic confinement is therefore needed to explain

the nonzero ϕ_0, and for this we turn to the impact of electrode-induced strain.

Strain develops in silicon MOS devices cooled to cryogenic temperatures [47,48] due to differences in the thermal contraction between metal electrodes and the silicon substrate. In particular, uniaxial strain alters the valence band heavy-hole–light-hole (HH-LH) splitting $\Delta_{\text{HH-LH}}$, while shear strains directly mix HH and LH components. Both can have an enormous influence on the composition of the confined hole state and its spin properties [57]. Figure 3(c) shows the spatial profile of $\Delta_{\text{HH-LH}}$ in the active region of the device. The HH-LH splitting varies by over 50% across the device and follows the lithography of the aluminum gate stack. The strain varies most rapidly at the edges and corners of the metal gates; shear strains concentrate there as well. Under the gates, biaxial compression by the shrinking metal pushes the LH basis states deeper in energy relative to HH states, i.e., acting in the same direction as the out-of-plane confinement. The impact of electrode-induced strain is particularly strong in these silicon MOS devices since the electrodes are separated by only 5.9 nm from the active charge region.

In an ideal device, the hole lies directly below the center of the G2 gate, as shown in Fig. 3. Figure 4(a) presents the simulated *g*-tensor surface of the single hole in its ground state (shaded blue surface). In this configuration the *g* tensor is as

expected for the predominantly HH-like state: The largest g factor occurs for a nearly out-of-plane magnetic field, with small but nonzero transverse components and tilt ϕ_0 of $8°$ due to the nonzero LH admixture. To tilt the hole g tensor significantly out of the 2D plane (i.e., $\phi_0 > 10°$), it is necessary to displace the hole wave function away from the point of near symmetry that occurs directly under a gate. This displacement can be due to atomic steps, surface charges, or other fluctuations of the Si/SiO$_2$ interface. A wave-function displacement is also realizable experimentally by altering the different gate biases, such as V_{G4}. Figure 4(c) presents the g-tensor surface simulated when the hole wave function is electrostatically displaced by about 15 nm to a region of highly nonuniform strain, as indicated in Fig. 4(d). The g-tensor surface in Fig. 4(c) is clearly tilted away from the Si/SiO$_2$ interface with $\phi_0 > 26°$.

Figure 4(e) shows the extracted tilt angle ϕ_0 of the g tensor as the hole is artificially being forced to various points along the sample x axis. The spatial dependence on ϕ_0 tracks the strain profile, responsible also for $\Delta_{\text{HH-LH}}$, shown in Fig. 4(f). When Bir-Pikus strain terms were omitted from the numerical model, the g-tensor tilting is suppressed, with a maximum $\phi_0 < 1°$. These simulations suggest that it is the nonuniform strain profile that causes the observed orientation of the g tensor to be misaligned from the electrostatic confinement orientation. In addition, residual strains associated with cryogenic cooling and/or processing have been discussed as a likely mechanism causing a discrepancy between the calculated and observed g tensor of holes in silicon-on-insulator (SOI) nanowire quantum dots [57].

Other plausible mechanisms, such as HH-LH mixing by the microscopically low-symmetry Si/SiO$_2$ interface [58], were evaluated and deemed insufficiently strong to significantly renormalize the hole state g tensor (see Sec. S2 of the Supplemental Material [50]).

III. CONCLUSIONS

In this paper we have experimentally studied the 3D g tensor of a single hole in a silicon-MOS-based quantum dot. We characterized the full 3D g tensor for two different bias configurations. Our results demonstrate strong electric control over both the magnitude and orientation of the single-hole g tensor.

A key experimental result is the wide range of control over the g factor, particularly the ability to configure a "sweet spot" where most components of dg/dV approach zero. For spin qubits, the coupling between hole spins and electric fields is a balancing act, where some large component of dg/dV maximizes the electric dipole spin resonance (EDSR) Rabi frequency. However, a large dg/dV also amplifies the impact of electrical noise leading to a shorter T_2^*. In the device under study we show that over a small range of bias configurations the hole can be tuned *in situ* to a region of high dg/dV, which is ideal for rapid spin manipulation, and then to a sweet spot where $dg/dV = 0$ for a dominant gate, which is ideal for long-lifetime qubit storage, prior to qubit readout [59].

Since these results are for a single hole, in the lowest quantum dot orbital state, it is possible to compare the experimental data with detailed theoretical models. These models suggest that electrode-induced strain has a significant effect on hole-spin states in quantum dots based on a p-type silicon MOS and show how the effects of strain vary dramatically as the hole wave function is moved around with gate biases.

We conclude that the effects of *nonuniform* strain are critical for understanding the single-hole g tensor, particularly in MOS devices. Furthermore, the impact of *nonuniform* electrode-induced strain is relevant to a wide variety of hole-spin-based devices. Therefore these results raise an interesting question: How effectively can the spatial strain profile be engineered to optimize the performance of hole-spin-based devices?

Finally, nonuniform electrode-induced strain is considered here as a mechanism enabling all electric spin manipulation of hole-based qubits. While overall strain has been used in spin-qubit devices [60,61], it has typically been used to engineer the static isotropic spin properties, particularly the HH-LH splitting. This work points to a potential technology for spin qubits, where specific gate geometries are designed to engineer *nonuniform* strain for optimized speed and performance.

APPENDIX A: SAMPLE DETAILS

The device studied in this paper was fabricated using the same processing procedure, but in a different processing run, as previous planar silicon hole quantum dot devices [46]. During operation the R gate is negatively biased to accumulate a 2D hole gas at the Si/SiO$_2$ interface below. A single quantum dot is defined by positively biasing gates G1, G3, and G4 and the C gate. Gate G2 acts as the dot plunger gate and is operated in the negatively biased regime. If gate G4 is made sufficiently negative, the device forms a double dot (see Sec. S7 of the Supplemental Material [50]). Full voltages are provided in Sec. S1 of the Supplemental Material [50]. The charge sensor is operated by negatively biasing the sensor top gate to facilitate hole transport. Sensor barrier gates, which are fabricated underneath the sensor top gate, are positively biased to form a region of high dI_{sens}/dV (either a quantum dot or sharp pinch-off) which is used to charge-sense the quantum dot below gate G2. We confirmed that the device operates down to a single hole using tunnel-rate-independent measurements.

APPENDIX B: MEASUREMENT DETAILS

All measurements were performed in a BlueFors XLD dilution refrigerator with a base temperature of 20 mK. For charge sensor measurements we monitor dI_{sens}/dV_{G2} using the standard dual lock-in technique with dynamic feedback to

optimize the charge sensor signal [62]. The charging energy and the *g* factors presented in Figs. 1 and 2 of the main text were extracted from the spacing in V_{G2} between the $N = 1$ and $N = 2$ Coulomb peaks [42]. The spacing in V_{G2} was then converted into energy using the lever arm, $\Delta E = \alpha_{G2} \Delta V_{G2}$, where $\alpha_{G2} = (0.166 \pm 0.007)$ eV/V. The full data set is presented in Sec. S4 of the Supplemental Material [50]. We have confirmed that the lever arm is independent of the gate voltages within the operating range of the experiment. For all rotation measurements we first confirm that $\Delta E(B)$ is linear in B up to 1 T for all directions.

For the rotation matrices in Eq. (1) we use the definition

$$R(\vartheta_0, \phi_0, \theta_0) = R_z(\theta_0)R_y(-\phi_0)R_z(\vartheta_0), \quad \text{(B1)}$$

where R_y and R_z are the standard 3D rotation matrices around the y and z axes.

APPENDIX C: MULTISCALE DEVICE MODELING INCLUDING STRAIN

For modeling the hole states, we use a custom numerical framework for the construction and multiscale simulations of the three-dimensional multilayer and multimaterial device model. Layout construction from production masks, with attention to their orientation with respect to the principal axes of the silicon substrate, is augmented by TEM data, process models, and known details of fabrication steps. To account for the stress which builds up when cooling the heterogeneous system to cryogenic temperatures, we solve the stationary stress-strain problem for the entire layout, assuming that the device is unstrained at the end of fabrication and that the device is free of any cracks or voids.

The obtained strain pattern can be combined with self-consistent Schrödinger-Poisson calculations, using a Thomas-Fermi approximation to model the partitioned two-dimensional hole gas accumulated outside the quantum region. The gate potentials for the Schrödinger-Poisson calculations are taken from those employed in the operation regime, including a global offset. Next, the single quantized hole in a Si complex valence band is treated quantum mechanically by solving, in three dimensions, the 6×6 Luttinger-Kohn Hamiltonian with Bir-Pikus strain terms, subject to realistic electrostatic confinement and strain. We extract the *g* tensor by evaluating splittings of the ground-state (or excited-state) doublet by the magnetic field at various angles relative to the simulated device.

In addition, modeling of the single-hole state has been conducted for a hypothetical 3D harmonic confinement. The hypothetical modeling is illuminating due to its much simplified parameter space of only three confinement strengths and three rotation angles. Further details are presented in Secs. S2 and S3 of the Supplemental Material [50].

APPENDIX D: ESTIMATION OF MINIMUM RABI FREQUENCY

To estimate a minimum Rabi frequency, we consider a 200-mT magnetic field, and a 4-mV ac signal applied to gate G4. We use Eq. (3) from Ref. [34]. We simplify this estimation by considering only the terms g_y and dg_y/dV_{G4} (i.e., naively considering that the tensor $\overleftrightarrow{g}$ and $d\overleftrightarrow{g}/dV_{G4}$ are diagonal in the measurement frame).

APPENDIX E: *g*-TENSOR DEFINITION AND FITTING PROCEDURE

In this paper we define the 3×3 *g* tensor, $\overleftrightarrow{g}$, using six parameters $(g_1, g_2, g_3, \vartheta_0, \phi_0, \theta_0)$ such that

$$\overleftrightarrow{g} = R_z(\vartheta_0)R_y(-\phi)R_z(\theta_0)\begin{pmatrix} g_1 & 0 & 0 \\ 0 & g_2 & 0 \\ 0 & 0 & g_3 \end{pmatrix}$$
$$\times R_z^{-1}(\theta_0)R_y^{-1}(-\phi_0)R_z^{-1}(\vartheta_0), \quad \text{(E1)}$$

where g_1, g_2, and g_3 are the principal *g*-factor values and θ_0, ϕ_0, and ϑ_0 define free rotations of the matrix allowing arbitrary orientation of the principal magnetic axes with respect to the sample (x, y, z) axes (the external frame of reference). Here, R_y and R_z are the standard rotation matrices around the y and z planes, respectively. Our convention is to use $R_y(-\phi_0)$ for rotation around the y axis.

To extract the hole *g* tensor, the full experimental data set is simultaneously fit to Eq. (E1). Below is the procedure used to fit all data to Eq. (E1). The procedure input takes experimental data points in a comma-separated value (csv) file with three columns: (1) θ, (2) ϕ, and (3) the observed *g* factor, where θ and ϕ define the applied magnetic field orientation (see Fig. 2 of the main text). Prior to fitting we apply the condition that $g_1 < g_2 < g_3$. The best-fit values of the *g*-tensor free parameters $(g_1, g_2, g_3, \vartheta_0, \phi_0, \theta_0)$ are presented in Table I of the main text.

The PYTHON notebook used for fitting the experimental *g*-factor data to Eq. (E1) of Appendix E can be found in the GitHub repository [63].

[1] D. Loss and D. P. DiVincenzo, Quantum computation with quantum dots, Phys. Rev. A **57**, 120 (1998).

[2] F. A. Zwanenburg, A. S. Dzurak, A. Morello, M. Y. Simmons, L. C. Hollenberg, G. Klimeck, S. Rogge, S. N. Coppersmith, and M. A. Eriksson, Silicon quantum electronics, Rev. Mod. Phys. **85**, 961 (2013).

[3] M. Veldhorst, H. Eenink, C.-H. Yang, and A. S. Dzurak, Silicon CMOS architecture for a spin-based quantum computer, Nat. Commun. **8**, 1766 (2017).

[4] G. Scappucci, C. Kloeffel, F. A. Zwanenburg, D. Loss, M. Myronov, J.-J. Zhang, S. De Franceschi, G. Katsaros, and M. Veldhorst, The germanium quantum information route, Nat. Rev. Mater. **6**, 926 (2020).

[5] L. Hutin, B. Bertrand, R. Maurand, A. Crippa, M. Urdampilleta, Y. Kim, A. Amisse, H. Bohuslavskyi, L. Bourdet, S. Barraud, X. Jeh, Y.-M. Niquet, M. Sanquer, C. Bäuerle, T. Meunier, S. De Franceschi, and M. Vinet, *Si MOS technology for spin-based quantum computing, in 2018 48th European Solid-State*

Device Research Conference (ESSDERC) (IEEE, Piscataway, NJ, 2018), pp. 12–17.

[6] R. Pillarisetty, N. Thomas, H. George, K. Singh, J. Roberts, L. Lampert, P. Amin, T. Watson, G. Zheng, J. Torres, M. Metz, R. Kotlyar, P. Keys, J. M. Boter, J. P. Dehollain, G. Droulers, G. Eenink, R. Li, L. Massa, D. Sabbagh *et al.*, *Qubit device integration using advanced semiconductor manufacturing process technology, in 2018 IEEE International Electron Devices Meeting (IEDM)* (IEEE, Piscataway, NJ, 2018), pp. 6.3.1–6.3.4.

[7] V. N. Golovach, M. Borhani, and D. Loss, Electric-dipole-induced spin resonance in quantum dots, Phys. Rev. B **74**, 165319 (2006).

[8] D. V. Bulaev and D. Loss, Electric Dipole Spin Resonance for Heavy Holes in Quantum Dots, Phys. Rev. Lett. **98**, 097202 (2007).

[9] P. Szumniak, S. Bednarek, B. Partoens, and F. Peeters, Spin-Orbit-Mediated Manipulation of Heavy-Hole Spin Qubits in Gated Semiconductor Nanodevices, Phys. Rev. Lett. **109**, 107201 (2012).

[10] R. Maurand, X. Jehl, D. Kotekar-Patil, A. Corna, H. Bohuslavskyi, R. Laviéville, L. Hutin, S. Barraud, M. Vinet, M. Sanquer, and S. De Franceschi, A CMOS silicon spin qubit, Nat. Commun. **7**, 13575 (2016).

[11] H. Watzinger, J. Kukučka, L. Vukušić, F. Gao, T. Wang, F. Schäffler, J.-J. Zhang, and G. Katsaros, A germanium hole spin qubit, Nat. Commun. **9**, 3902 (2018).

[12] D. Jirovec, A. Hofmann, A. Ballabio, P. M. Mutter, G. Tavani, M. Botifoll, A. Crippa, J. Kukucka, O. Sagi, and F. Martins, J. Saez-Mollejo, I. Prieto, M. Borovkov, J. Arbiol, D. Chrastina, G. Isella, and G. Katsaros, A singlet-triplet hole spin qubit in planar Ge, Nat. Mater. **20**, 1106 (2021).

[13] N. Hendrickx, D. Franke, A. Sammak, G. Scappucci, and M. Veldhorst, Fast two-qubit logic with holes in germanium, Nature (London) **577**, 487 (2020).

[14] N. Hendrickx, W. Lawrie, L. Petit, A. Sammak, G. Scappucci, and M. Veldhorst, A single-hole spin qubit, Nat. Commun. **11**, 3478 (2020).

[15] N. W. Hendrickx, W. I. Lawrie, M. Russ, F. van Riggelen, S. L. de Snoo, R. N. Schouten, A. Sammak, G. Scappucci, and M. Veldhorst, A four-qubit germanium quantum processor, Nature (London) **591**, 580 (2021).

[16] R. Hanson, L. P. Kouwenhoven, J. R. Petta, S. Tarucha, and L. M. Vandersypen, Spins in few-electron quantum dots, Rev. Mod. Phys. **79**, 1217 (2007).

[17] R. Winkler, S. Papadakis, E. De Poortere, and M. Shayegan, Spin-orbit coupling in two-dimensional electron and hole systems, in *Advances in Solid State Physics*, Advances in Solid State Physics Vol. 41 (Springer, New York, 2003), pp. 211–223.

[18] D. V. Bulaev and D. Loss, Spin Relaxation and Decoherence of Holes in Quantum Dots, Phys. Rev. Lett. **95**, 076805 (2005).

[19] S. Chesi, X. J. Wang, and W. Coish, Controlling hole spins in quantum dots and wells, Eur. Phys. J. Plus **129**, 86 (2014).

[20] D. Q. Wang, O. Klochan, J.-T. Hung, D. Culcer, I. Farrer, D. A. Ritchie, and A. R. Hamilton, Anisotropic Pauli spin blockade of holes in a GaAs double quantum dot, Nano Lett. **16**, 7685 (2016).

[21] D. Miserev, A. Srinivasan, O. Tkachenko, V. Tkachenko, I. Farrer, D. Ritchie, A. Hamilton, and O. Sushkov, Mechanisms for Strong Anisotropy of In-Plane *g*-Factors in Hole Based Quantum Point Contacts, Phys. Rev. Lett. **119**, 116803 (2017).

[22] D. Miserev and O. Sushkov, Dimensional reduction of the Luttinger Hamiltonian and *g*-factors of holes in symmetric two-dimensional semiconductor heterostructures, Phys. Rev. B **95**, 085431 (2017).

[23] M. Schroer, K. Petersson, M. Jung, and J. R. Petta, Field Tuning the *g* Factor in InAs Nanowire Double Quantum Dots, Phys. Rev. Lett. **107**, 176811 (2011).

[24] S. Takahashi, R. Deacon, A. Oiwa, K. Shibata, K. Hirakawa, and S. Tarucha, Electrically tunable three-dimensional *g*-factor anisotropy in single InAs self-assembled quantum dots, Phys. Rev. B **87**, 161302(R) (2013).

[25] J. C. H. Chen, O. Klochan, A. P. Micolich, A. R. Hamilton, T. P. Martin, L. H. Ho, U. Zülicke, D. Reuter, and A. D. Wieck, Observation of orientation- and *k*-dependent Zeeman spin-splitting in hole quantum wires on (100)-oriented AlGaAs/GaAs heterostructures, New J. Phys. **12**, 033043 (2010).

[26] N. Ares, V. Golovach, G. Katsaros, M. Stoffel, F. Fournel, L. Glazman, O. Schmidt, and S. De Franceschi, Nature of Tunable Hole *g* Factors in Quantum Dots, Phys. Rev. Lett. **110**, 046602 (2013).

[27] F. A. Zwanenburg, C. E. van Rijmenam, Y. Fang, C. M. Lieber, and L. P. Kouwenhoven, Spin states of the first four holes in a silicon nanowire quantum dot, Nano Lett. **9**, 1071 (2009).

[28] J. Van der Heijden, J. Salfi, J. A. Mol, J. Verduijn, G. C. Tettamanzi, A. R. Hamilton, N. Collaert, and S. Rogge, Probing the spin states of a single acceptor atom, Nano Lett. **14**, 1492 (2014).

[29] A. Srinivasan, K. Hudson, D. Miserev, L. Yeoh, O. Klochan, K. Muraki, Y. Hirayama, O. Sushkov, and A. Hamilton, Electrical control of the sign of the *g* factor in a GaAs hole quantum point contact, Phys. Rev. B **94**, 041406(R) (2016).

[30] B. Voisin, R. Maurand, S. Barraud, M. Vinet, X. Jehl, M. Sanquer, J. Renard, and S. De Franceschi, Electrical control of *g*-factor in a few-hole silicon nanowire MOSFET, Nano Lett. **16**, 88 (2016).

[31] A. Bogan, S. A. Studenikin, M. Korkusinski, G. Aers, L. Gaudreau, P. Zawadzki, A. S. Sachrajda, L. Tracy, J. Reno, and T. Hargett, Consequences of Spin-Orbit Coupling at the Single Hole Level: Spin-Flip Tunneling and the Anisotropic *g* Factor, Phys. Rev. Lett. **118**, 167701 (2017).

[32] S. Studenikin, M. Korkusinski, M. Takahashi, J. Ducatel, A. Padawer-Blatt, A. Bogan, D. G. Austing, L. Gaudreau, P. Zawadzki, A. Sachrajda, Y. Hirayama, L. Tracy, J. Reno, and T. Hargett, Electrically tunable effective *g*-factor of a single hole in a lateral GaAs/AlGaAs quantum dot, Commun. Phys. **2**, 159 (2019).

[33] T. Tanttu, B. Hensen, K. W. Chan, C. H. Yang, W. W. Huang, M. Fogarty, F. Hudson, K. Itoh, D. Culcer, A. Laucht, A. Morello, and A. Dzurak, Controlling Spin-Orbit Interactions in Silicon Quantum Dots Using Magnetic Field Direction, Phys. Rev. X **9**, 021028 (2019).

[34] A. Crippa, R. Maurand, L. Bourdet, D. Kotekar-Patil, A. Amisse, X. Jehl, M. Sanquer, R. Laviéville, H. Bohuslavskyi, L. Hutin, S. Barraud, M. Vinet, Y.-M. Niquet, and S. De Franceschi, Electrical Spin Driving by *g*-Matrix Modulation in Spin-Orbit Qubits, Phys. Rev. Lett. **120**, 137702 (2018).

[35] Y. Hu, F. Kuemmeth, C. M. Lieber, and C. M. Marcus, Hole spin relaxation in Ge–Si core–shell nanowire qubits, Nat. Nanotechnol. **7**, 47 (2012).

[36] N. Ares, G. Katsaros, V. N. Golovach, J. Zhang, A. Prager, L. I. Glazman, O. G. Schmidt, and S. De Franceschi, SiGe quantum dots for fast hole spin Rabi oscillations, Appl. Phys. Lett. **103**, 263113 (2013).

[37] M. Brauns, J. Ridderbos, A. Li, E. P. Bakkers, and F. A. Zwanenburg, Electric-field dependent *g*-factor anisotropy in Ge-Si core-shell nanowire quantum dots, Phys. Rev. B **93**, 121408(R) (2016).

[38] H. Watzinger, C. Kloeffel, L. Vukusic, M. D. Rossell, V. Sessi, J. Kukucka, R. Kirchschlager, E. Lausecker, A. Truhlar, M. Glaser, A. Rastelli, A. Fuhrer, D. Loss, and G. Katsaros, Heavy-hole states in germanium hut wires, Nano Lett. **16**, 6879 (2016).

[39] A. Crippa, R. Ezzouch, A. Aprá, A. Amisse, R. Laviéville, L. Hutin, B. Bertrand, M. Vinet, M. Urdampilleta, T. Meunier, M. Sanquer, X. Jehl, R. Maurand, and S. De Franceschi, Gate-reflectometry dispersive readout and coherent control of a spin qubit in silicon, Nat. Commun. **10**, 2776 (2019).

[40] M. Marx, J. Yoneda, Á. G. Rubio, P. Stano, T. Otsuka, K. Takeda, S. Li, Y. Yamaoka, T. Nakajima, A. Noiri, D. Loss, T. Kodera, and S. Tarucha, Spin orbit field in a physically defined p type MOS silicon double quantum dot, arXiv:2003.07079.

[41] S. Geyer, L. C. Camenzind, L. Czornomaz, V. Deshpande, A. Fuhrer, R. J. Warburton, D. M. Zumbühl, and A. V. Kuhlmann, Self-aligned gates for scalable silicon quantum computing, Appl. Phys. Lett. **118**, 104004 (2021).

[42] L. P. Kouwenhoven, D. Austing, and S. Tarucha, Few-electron quantum dots, Rep. Prog. Phys. **64**, 701 (2001).

[43] R. Li, F. E. Hudson, A. S. Dzurak, and A. R. Hamilton, Single hole transport in a silicon metal-oxide-semiconductor quantum dot, Appl. Phys. Lett. **103**, 163508 (2013).

[44] P. C. Spruijtenburg, J. Ridderbos, F. Mueller, A. W. Leenstra, M. Brauns, A. A. Aarnink, W. G. van der Wiel, and F. A. Zwanenburg, Single-hole tunneling through a two-dimensional hole gas in intrinsic silicon, Appl. Phys. Lett. **102**, 192105 (2013).

[45] R. Li, F. E. Hudson, A. S. Dzurak, and A. R. Hamilton, Pauli spin blockade of heavy holes in a silicon double quantum dot, Nano Lett. **15**, 7314 (2015).

[46] S. Liles, R. Li, C. Yang, F. Hudson, M. Veldhorst, A. S. Dzurak, and A. Hamilton, Spin and orbital structure of the first six holes in a silicon metal-oxide-semiconductor quantum dot, Nat. Commun. **9**, 3255 (2018).

[47] T. Thorbeck and N. M. Zimmerman, Formation of strain-induced quantum dots in gated semiconductor nanostructures, AIP Adv. **5**, 087107 (2015).

[48] J. Park, Y. Ahn, J. Tilka, K. Sampson, D. Savage, J. R. Prance, C. Simmons, M. Lagally, S. Coppersmith, M. Eriksson, M. V. Holt, and P. G. Evans, Electrode-stress-induced nanoscale disorder in Si quantum electronic devices, APL Mater. **4**, 066102 (2016).

[49] S. J. Angus, A. J. Ferguson, A. S. Dzurak, and R. G. Clark, Gate-defined quantum dots in intrinsic silicon, Nano Lett. **7**, 2051 (2007).

[50] See Supplemental Material at http://link.aps.org/supplemental/10.1103/PhysRevB.104.235303 for details.

[51] W. I. L. Lawrie, N. W. Hendrickx, F. van Riggelen, M. Russ, L. Petit, A. Sammak, G. Scappucci, and M. Veldhorst, Spin relaxation benchmarks and individual qubit addressability for holes in quantum dots, Nano Lett. **20**, 7237 (2020).

[52] Y. Kato, R. Myers, D. Driscoll, A. Gossard, J. Levy, and D. Awschalom, Gigahertz electron spin manipulation using voltage-controlled g-tensor modulation, Science **299**, 1201 (2003).

[53] T. Kobayashi, J. Salfi, C. Chua, J. van der Heijden, M. G. House, D. Culcer, W. D. Hutchison, B. C. Johnson, J. C. McCallum, H. Riemann, N. V. Abrosimov, P. Becker, H.-J. Pohl, M. Y. Simmons, and S. Rogge, Engineering long spin coherence times of spin–orbit qubits in silicon, Nat. Mater. **20**, 38 (2020).

[54] Z. Wang, E. Marcellina, A. R. Hamilton, J. H. Cullen, S. Rogge, J. Salfi, and D. Culcer, Optimal operation points for ultrafast, highly coherent Ge hole spin-orbit qubits, npj Quantum Inf. **7**, 54 (2021).

[55] S. Bosco, B. Hetényi, and D. Loss, Hole Spin Qubits in Si FinFETs with Fully Tunable Spin-Orbit Coupling and Sweet Spots for Charge Noise, PRX Quantum **2**, 010348 (2021).

[56] C. Adelsberger, M. Benito, S. Bosco, J. Klinovaja, and D. Loss, Hole spin qubits in Ge nanowire quantum dots: Interplay of orbital magnetic field, strain, and growth direction, arXiv:2110.15039.

[57] B. Venitucci, L. Bourdet, D. Pouzada, and Y.-M. Niquet, Electrical manipulation of semiconductor spin qubits within the *g*-matrix formalism, Phys. Rev. B **98**, 155319 (2018).

[58] A. Y. K. E. L. Ivchenko and U. Rössler, Heavy-light hole mixing at zinc-blende (001) interfaces under normal incidence, Phys. Rev. B **54**, 5852 (1996).

[59] F. N. Froning, L. C. Camenzind, O. A. van der Molen, A. Li, E. P. Bakkers, D. M. Zumbühl, and F. R. Braakman, Ultrafast hole spin qubit with gate-tunable spin–orbit switch functionality, Nat. Nanotechnol. **16**, 308 (2021).

[60] A. Dobbie, M. Myronov, R. Morris, A. Hassan, M. Prest, V. Shah, E. Parker, T. Whall, and D. Leadley, Ultra-high hole mobility exceeding one million in a strained germanium quantum well, Appl. Phys. Lett. **101**, 172108 (2012).

[61] N. Hendrickx, D. Franke, A. Sammak, M. Kouwenhoven, D. Sabbagh, L. Yeoh, R. Li, M. Tagliaferri, M. Virgilio, G. Capellini, G. Scappucci, and M. Veldhorst, Gate-controlled quantum dots and superconductivity in planar germanium, Nat. Commun. **9**, 2835 (2018).

[62] C. Yang, W. Lim, F. Zwanenburg, and A. Dzurak, Dynamically controlled charge sensing of a few-electron silicon quantum dot, AIP Adv. **1**, 042111 (2011).

[63] https://github.com/ScottDLiles/gFactorFitting.git.